Proceedings of the EuroGNC 2013, 2nd CEAS Specialist Conference
on Guidance, Navigation & Control, Delft University of Technology,
Delft, The Netherlands, April 10-12, 2013



# Adaptive Augmentation of a Fighter Aircraft Autopilot Using a Nonlinear Reference Model

**Miguel Leitão, Florian Peter, and Florian Holzapfel**

**Abstract.** A Nonlinear Dynamic Inversion (NDI) baseline control architecture based on a nonlinear reference model and augmented by an adaptive element is developed for an agile modern fighter aircraft. This paper mainly focuses on the nonlinear reference model and on a modified NDI error feedback architecture. The chosen reference model contains the main nonlinear plant characteristics and is therefore able to fully exploit the physical capabilities of the fighter aircraft. Starting with the classical inversion control laws, the implemented NDI-based error feedback baseline controller architecture is tailored according to the modifications motivated by the new reference model. In order to keep closed-loop performance in the vicinity of the nominal case, even in the presence of severe uncertainties and turbulence, the aforementioned baseline controller is augmented by an adaptive layer. The employed control architecture has proven its capabilities and its robustness for a large set of uncertainties and in the presence of turbulence effects.

## Nomenclature

| | |
|---|---|
| $\mathbf{A}(\boldsymbol{x})$ | Decoupling matrix of the body-rates and outer dynamics |
| $\left(\boldsymbol{a}_K^G\right)_B$ | $\left[a_x^G \quad a_y^G \quad a_z^G\right]_B^T$ Acceleration due to kinematic forces at the CG denoted in the *B*-Frame |
| $\boldsymbol{b}(\boldsymbol{x})$ | Nonlinearities of the body-rates and outer dynamics |
| $C_{i_J}$ | Aerodynamic coefficient |
| $\boldsymbol{e}$ | Error variable |
| $\boldsymbol{F}_I, \boldsymbol{F}_O$ | Mapping of the inner and outer loop dynamics |
| $\left(\boldsymbol{F}_T^G\right)_B$ | $[X_T^G \quad Y_T^G \quad Z_T^G]_B^T$ Total force applied at the CG and denoted in the *B*-Frame |
| $\left(\mathbf{I}^G\right)_{BB}$ | Moment of inertia given in the *B*-Frame |
| $\boldsymbol{K}$ | Constant feedback gain |
| $l$ | Reference length |
| $m$ | Aircraft mass |
| $\boldsymbol{M}_{OB}$ | Transformation matrix from *B*-Frame to *O*-Frame |
| $\left(\boldsymbol{M}_T^G\right)_B$ | $[L_T^G \quad M_T^G \quad N_T^G]_B^T$ Total moments applied at the CG and denoted in the *B*-Frame |

Miguel Leitão · Florian Peter · Florian Holzapfel
Institute of Flight System Dynamics, TU München, Boltzmannstr. 15, 85748 Garching, Germany
E-mail: Miguel.Leitao@tum.de, Florian.Peter@tum.de, Florian.Holzapfel@tum.de

| | |
|---|---|
| $\bar{q}$ | Dynamic pressure |
| $(\boldsymbol{q})_B$ | Quaternion vector |
| $(\boldsymbol{r}^G)_O$ | $[x^G \quad y^G \quad z^G]_O^T$ Position vector of the CG given in the $O$-Frame |
| $S$ | Wing reference area |
| $\boldsymbol{u}_C$ | Commanded plant input vector |
| $\left(\boldsymbol{V}_K^G\right)_B^O$ | $[u_K^G \quad v_K^G \quad w_K^G]_B^{T,O}$ Kinematic velocity vector given in the $B$-Frame |
| $\boldsymbol{y}_C$ | Command vector |
| $\alpha_A, \beta_A$ | Aerodynamic angle of attack, aerodynamic sideslip angle |
| $\boldsymbol{\Gamma_e}, \boldsymbol{\Gamma_\varphi}$ | Learning rates for error feedback gains and estimated plant parameters |
| $\delta_T$ | Throttle level state |
| $\boldsymbol{\Delta_\omega}, \boldsymbol{\Delta_O}$ | Uncertainty of the inner and outer dynamics |
| $\zeta, \xi_L, \xi_R$ | Rudder, left aileron and right aileron deflections |
| $\Theta, \Phi, \Psi$ | Euler angles: pitch, roll and yaw angles |
| $\boldsymbol{\Theta}^*$ | Ideal, unknown system parameter |
| $\boldsymbol{\nu}$ | Pseudo-control |
| $\boldsymbol{\varphi}(\boldsymbol{x})$ | Nonlinear Regressor Vector |
| $\left(\boldsymbol{\omega}_K^{OB}\right)_B$ | $[p_K \quad q_K \quad r_K]_B^T$ Kinematic angular rates given in the $B$-Frame |

# 1 Introduction

Modern fighter aircraft must fulfill demanding performance requirements, which include aggressive maneuvering under harsh flight conditions. The main challenge in designing Flight Control Systems (FCS) for such platforms is therefore to achieve the maximum performance they are capable of, maintaining the desired robustness.

Nonlinear Dynamic Inversion is a well-known technique when considering the design of nonlinear flight controllers, which can be applied to highly agile aerospace applications, such as fighter aircraft. This approach has successfully proven its capabilities in several theoretical frameworks [1-3] and flight tests [4-6]. The basic NDI feedback structure is able to transform the plant into a linear time invariant system (by cancelling the nonlinear system dynamics) on which known control methods which require linear systems can then be applied. This strategy can make use of reference models, which basically act as command filters whose main function is to provide the FCS with reference signals that can be effectively tracked without exceeding the plant capabilities. Most of the current research frameworks involving NDI and aerial applications make use of linear reference models [3, 7, 8]. However, the use of linear reference models in highly nonlinear systems such as modern fighter aircraft, forces these platforms into a linear behavior which does not match their dynamics. This means that the flight controller is not taking advantage of the full physical capabilities of the aerial vehicle [9].

In order to successfully cancel the system dynamics via NDI, a very accurate plant model is required. Due to the inherent complex aerodynamics of aerial vehicles, the modeling task is often a source of significant uncertainties. Such discrepancies between real and modeled plant dynamics may lead to performance degradation. Another drawback of classic NDI is the fact that the system states, necessary for canceling the nonlinearities, are often not fully measurable or biased by measurement noise and errors. Additionally, the actuator dynamics and inherent saturation effects are often neglected during the control design task, which might limit system performance and deteriorate robustness. Some of the abovementioned problems can be avoided by making use of a nonlinear reference model which includes the main nonlinear plant characteristics [9]. This reference model is capable of "shaping" the command signal so that the plant can perfectly track it under nominal conditions, which reduces the workload of the error controller.

Unlike baseline controllers which are based on the classical NDI approach [6, 7], the framework discussed herein makes use of a modified NDI architecture incorporating a linear error feedback controller which has been designed by taking the nonlinear reference model structure into account. Moreover, in order to preserve nominal closed-loop performance even in the presence of a large spectrum of uncertainties, the controller is augmented with an adaptive element based on Model Reference Adaptive Control (MRAC) [10]. The nominal closed-loop error dynamics exhibit an almost linear characteristic, which makes MRAC the perfect choice to perform adaptive augmentation. This adaptive control strategy is able to cancel the uncertainties which remain after NDI has been applied, maintaining an adequate performance, even in case large plant degradations occur [9].

A generic realistic nonlinear six degree-of-freedom (6DOF) modern fighter aircraft model has been used to demonstrate the benefits and usefulness of the suggested approach. The controller performance is evaluated for an aggressive maneuver involving the longitudinal and lateral control channels. This maneuver has been carried out under harsh conditions, e.g. in the presence of large uncertainties and strong turbulence effects.

## 2 Fighter Aircraft Model

This chapter introduces the main features of the simulation model by presenting the employed equations of motion, and by providing some information concerning different aircraft subsystems. The chosen 6DOF model is based on the nonlinear dynamics of a delta-wing single-engine modern fighter aircraft flying in a clean configuration (there are no stores and the landing gear is retracted). It assumes that there are no canards, no air brakes, and that thrust vectoring is not available.

The modeled aircraft can be controlled via four control devices: its single engine (throttle position given by $\delta_T$) and its three control surfaces (left elevon deflection $\xi_L$, right elevon deflection $\xi_R$ and rudder deflection $\zeta$). Since the elevons

can be symmetrically or asymmetrically deflected in order to respectively induce pitch or roll maneuvers, a new representation for the control surface deflections is required. The pitch ($\delta_M$), roll ($\delta_L$) and yaw ($\delta_N$) input variables are given by the following linear mapping:

$$\begin{bmatrix}\delta_L\\ \delta_M\\ \delta_N\end{bmatrix} = \frac{1}{2}\begin{bmatrix}(\xi_R - \xi_L)\\ (\xi_R + \xi_L)\\ 2\zeta\end{bmatrix}. \tag{1}$$

The engine dynamics are modeled by a constant time delay and by a first-order lag. The total thrust force is given by a linear function depending on the throttle position, the static pressure $p_S$, the Mach number Ma and on the aircraft altitude $z_O^G$. The three control surface actuators are nonreversible and modeled by second-order linear systems with acceleration, rate and position limits. The elevon actuator dynamics take some aeroelasticity effects into account, namely the influence of the hinge moments acting on the control surface.

Regarding the aircraft rigid-body dynamics, the simulation model makes use of two fundamental reference frames: the Body-Fixed frame ($B$-frame) and the North-East-Down (NED) frame ($O$-frame). The $B$-frame moves with the aircraft and its origin is located at the aircraft Centre of Gravity (CG) with the $x$-axis coincident with the Fuselage Reference Line and positive towards the aircraft nose. It must be noticed that the equations of motion included in the model are based on the "flat and non-rotating Earth" assumption. Moreover, the gravity acceleration vector is vertical and has a constant modulus. The aircraft rigid-body motion is defined by the translational, rotational, attitude and position dynamics, which are respectively given by the following differential equations:

$$\left(\dot{\boldsymbol{V}}_K^G\right)_B^{OB} = \frac{1}{m}\cdot(\boldsymbol{F}_T^G)_B - (\boldsymbol{\omega}_K^{OB})_B \times (\boldsymbol{V}_K^G)_B^O \tag{2}$$

$$(\dot{\boldsymbol{\omega}}_K^{OB})_B^B = (\mathbf{I}^G)_{BB}^{-1}\cdot[(\boldsymbol{M}_T^G)_B - (\boldsymbol{\omega}_K^{OB})_B \times (\mathbf{I}^G)_{BB}\cdot(\boldsymbol{\omega}_K^{OB})_B] \tag{3}$$

$$(\dot{\boldsymbol{q}})_B = \frac{1}{2}\cdot(\boldsymbol{q})_B \circ (\boldsymbol{\omega}_K^{OB})_B \tag{4}$$

$$(\dot{\boldsymbol{r}}^G)_O^O = \mathbf{M}_{EB}\cdot(\boldsymbol{V}_K^G)_B^O, \tag{5}$$

where $\circ$ denotes the quaternion product and $\mathbf{M}_{OB}$ is the transformation matrix which converts a vector defined in the $B$-frame into the $O$-frame.

The total forces and moments comprised in expressions (2) and (3) encompass the influence of gravity, propulsion and aerodynamic effects. The simulation model neglects the moments generated by the aircraft engine and thus $(\boldsymbol{M}_P^G)_B = \mathbf{0}$. The assembly of total forces and moments given in the $B$-frame is depicted in equations (6) and (7), respectively.

$$(\boldsymbol{F}_T^G)_B = \bar{q} \cdot S \cdot \begin{bmatrix} C_X \\ C_Y \\ C_Z \end{bmatrix}_B^R + \begin{bmatrix} T \\ 0 \\ 0 \end{bmatrix}_B^G + m \cdot g \cdot \begin{bmatrix} \sin\Theta \\ \cos\Theta \cdot \sin\Phi \\ \cos\Theta \cdot \cos\Phi \end{bmatrix} \tag{6}$$

$$(\boldsymbol{M}_T^G)_B = \bar{q} \cdot S \cdot l \cdot \begin{bmatrix} C_L \\ C_M \\ C_N \end{bmatrix}_B^R + \boldsymbol{r}^{GR} \times \left( \bar{q} \cdot S \cdot \begin{bmatrix} C_X \\ C_Y \\ C_Z \end{bmatrix}_B^R \right) \tag{7}$$

In the expressions above, $\bar{q}$ represents the dynamic pressure, $S$ is the reference area, $l$ the reference length, $T$ the total thrust force, $m$ the aircraft mass, $g$ the constant gravity acceleration, and $\boldsymbol{r}^{GR}$ is the relative position between aerodynamic reference point and center of gravity. Taking the application rule of the generic aerodynamic data set into account, the different aerodynamic coefficients defined with respect to the aerodynamic reference point are given by the following six expressions:

$$C_X = C_{X\alpha}(\alpha, \mathrm{Ma}) \tag{8}$$

$$C_Y = CY_\beta(\mathrm{Ma}) \cdot \beta + C_{Y\delta_N}(\mathrm{Ma}) \cdot \delta_N \tag{9}$$

$$C_Z = C_{Z\alpha}(\mathrm{Ma}) \cdot \alpha + C_{Z\delta_M}(\mathrm{Ma}) \cdot \delta_M \tag{10}$$

$$C_L = C_{L\beta}(\alpha) \cdot \beta + C_{L\delta_L}(\mathrm{Ma}) \cdot \delta_L + C_{L\delta_N}(\mathrm{Ma}) \cdot \delta_N + \frac{l}{V_{TAS}}\left[p \cdot C_{Lp} + r \cdot C_{Lr}\right] \tag{11}$$

$$C_M = C_{M\alpha}(\mathrm{Ma}) \cdot \alpha + C_{M\delta_M}(\mathrm{Ma}) \cdot \delta_M + q \cdot \frac{l}{V_{TAS}} \cdot C_{Mq} \tag{12}$$

$$C_N = C_{N\beta}(\mathrm{Ma}) \cdot \beta + C_{N\delta_L}(\mathrm{Ma}) \cdot \delta_L + C_{N\delta_N}(\mathrm{Ma}) \cdot \delta_N + \frac{l}{V_{TAS}}\left[p \cdot C_{Np} + r \cdot C_{Nr}\right]. \tag{13}$$

In order to properly compute the necessary atmospheric properties, this framework makes use of a static model based on a simplified version of the U.S. Standard Atmosphere 1976 [11]. It is able to model constant and dynamic wind effects as it contains a simplified 3-axes Dryden turbulence model whose parameters are defined as a function of the aircraft altitude and velocity. The expression below shows the direct influence of the wind effects on the aerodynamic velocity vector.

$$\boldsymbol{V}_A^G = \boldsymbol{V}_K^G + \boldsymbol{V}_W^G \tag{14}$$

The fighter aircraft model simulates three different sensor systems: a probe (measuring the aerodynamic angle of attack $\alpha_A$ and the sideslip angle $\beta_A$), an Air Data System (which acquires the True Airspeed $V_{TAS}$, the Mach number, the Calibrated Airspeed $V_{CAS}$ and the dynamic and static pressures), and an Inertial Measurement Unit (responsible for measuring the aircraft altitude, the angular rates

$(\boldsymbol{\omega}_K)_B$, the Euler angles $\Phi, \Theta$ and $\Psi$, and the linear accelerations in the $B$-frame). All sensors are located at the aircraft CG except for the accelerometers, which are placed ahead of the aerodynamic reference point. The modeled sensors are considered to be ideal, meaning that the simulation framework does not account for any bias, measurement noise or even sensor dynamics.

## 3 Flight Control System Design

This section describes the core task of this research framework, namely the design and development of an adaptive flight control system for the nonlinear fighter aircraft model introduced in the previous chapter. In order to achieve desired closed-loop performance by fully exploiting the aerial vehicle's physical capabilities, a NDI-based baseline controller which makes use of a nonlinear reference model has been implemented [9]. Since the main objective is to ensure aircraft stability and maneuverability, even under the presence of turbulence and harsh uncertainties, the aforementioned baseline controller has been augmented with an adaptive layer based on the MRAC theory [10]. Figure 1 depicts the implemented flight control system architecture and the main FCS components which will be thoroughly clarified on the remainder of this document.

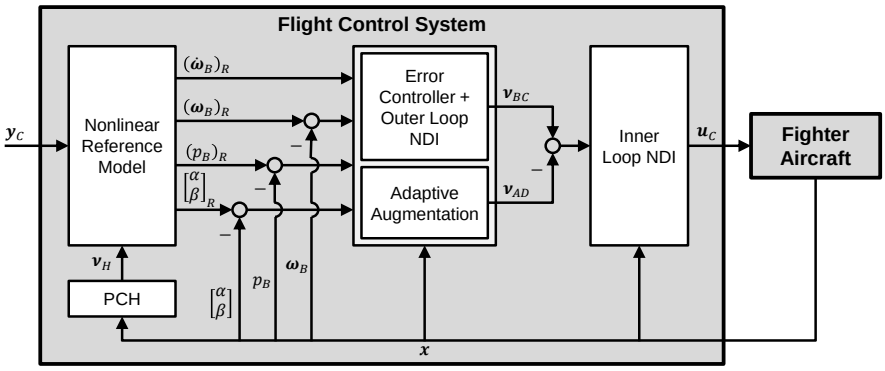


**Fig. 1** Flight Control System Architecture

This chapter starts by introducing the model which has been used for control design purposes (it is also the underlying structure of the nonlinear reference model). Additionally, the implemented reference model and the necessary modifications to the classical NDI-based baseline controller motivated by the employed control approach are explained in detail. Its final section is entirely dedicated to the adaptive augmentation of the abovementioned baseline controller.

### *3.1 Model Used for Control Design*

Since not all aircraft states are available to the controller, an alternative less complex representation of the plant is required for control design purposes (different from equations (2) to (5)). The implemented nonlinear reference model defined on the next section will also benefit from this representation. In order to demonstrate the potential of the chosen control approach, three control variables (corresponding to the roll, pitch and yaw control channels) have been provided. These variables form the so-called command vector $\boldsymbol{y}_C$, which is defined as follows:

$$\boldsymbol{y}_C = \begin{bmatrix} (p_K)_S \\ \alpha_A \\ \beta_A \end{bmatrix}_C . \tag{15}$$

In the definition above, $(p_K)_S$ denotes the roll rate in the stability axis, whereas $\alpha_A, \beta_A$ respectively represent the aerodynamic angle of attack and the aerodynamic sideslip angle. The stability axis frame ($S$-frame) has its origin at the aircraft reference point, moving with it, and rotating with the direction of airflow relative to the airplane.

Whereas the roll rate $(p_K)_S$ belongs to the fast inner plant dynamics (3), the aerodynamic angles $\alpha_A$ and $\beta_A$ are part of the slower outer plant dynamics (2). Therefore, a more compact plant representation considering a two-dimensional outer dynamic layer (comprising the angle of attack and sideslip angle dynamics) and a three-dimensional inner layer (comprising the rotational dynamics defined in the body-fixed frame) has been chosen. The outer layer dynamics and the rotational (inner) dynamics can be represented in the following form:

$$\boldsymbol{F}_O: \quad \dot{\boldsymbol{y}} = \begin{bmatrix} \dot{\alpha}_A \\ \dot{\beta}_A \end{bmatrix} = \mathbf{A}_O \cdot \begin{bmatrix} (q_K) \\ (r_K) \end{bmatrix}_S + \boldsymbol{b}_O, \tag{16}$$

$$\boldsymbol{F}_I: \quad \dot{\boldsymbol{\omega}}_B = \mathbf{A}_I \cdot \boldsymbol{u}_C + \boldsymbol{b}_I, \tag{17}$$

where $\mathbf{A}_O \in \mathbb{R}^{2\times2}, \mathbf{A}_I \in \mathbb{R}^{3\times3}$ are the so-called decoupling matrices, $\boldsymbol{b}_O \in \mathbb{R}^{2\times1}, \boldsymbol{b}_I \in \mathbb{R}^{3\times1}$ are vectors which contain the nonlinearities, $\boldsymbol{u}_C \in \mathbb{R}^{3\times1}$ is the plant input vector, and the indexes *O* and *I* respectively represent the outer and inner dynamic layers. The full dynamics of each layer are contained in the respective mappings $\boldsymbol{F}_O, \boldsymbol{F}_I$. Since the model used by the controller is subject to uncertainties and modeling errors, a distinction between nominal and estimated dynamics must be made. The uncertain approximations of $\mathbf{A}$, $\boldsymbol{b}$ and $\boldsymbol{F}$ are respectively given by $\widehat{\mathbf{A}}$, $\widehat{\boldsymbol{b}}$ and $\widehat{\boldsymbol{F}}$.

From expressions (16) and (17), it can be seen that the angular rates from the inner and outer layers are not defined in a common reference frame. Due to this

fact, the model comprised in the FCS connects the two dynamic layers making use of the transformation matrix $\mathbf{M}_{BS}$ (transformation from $S$-frame into the $B$-frame).

$$\boldsymbol{\omega}_B = \mathbf{M}_{BS} \cdot \boldsymbol{\omega}_S = \begin{bmatrix} \cos\alpha & 0 & -\sin\alpha \\ 0 & 1 & 0 \\ \sin\alpha & 0 & \cos\alpha \end{bmatrix} \cdot \boldsymbol{\omega}_S \tag{18}$$

Once again, it is known that the complete state vector is not available to the flight controller (e.g. the available sensors are not able to measure the complete velocity vector $\boldsymbol{V}_K^G$). Therefore, an alternative representation to the translational equations of motion given by (2) has been selected. Expression (19) provides the outer layer dynamics, which are necessary to estimate $\dot{\boldsymbol{y}}$ at the FCS level.

$$\begin{bmatrix} \dot{\alpha} \\ \dot{\beta} \end{bmatrix} = \begin{bmatrix} \frac{Z_{\bar{K}}}{m \cdot V_{TAS} \cdot \cos\beta} + (q_K)_S - (p_K)_S \cdot \tan\beta \\ \frac{Y_{\bar{K}}}{m \cdot V_{TAS}} - (r_K)_S \end{bmatrix} \tag{19}$$

In the expression above, $Y_{\bar{K}}$ and $Z_{\bar{K}}$ respectively represent the lateral and vertical forces defined on the rotated kinematic frame. These forces can be obtained from the accelerometer measurements $(\boldsymbol{a}_K^G)_B^{EB}$ via the transformation matrix $\mathbf{M}_{\bar{K}B}$. The rotated kinematic frame ($\bar{K}$-frame) is basically the kinematic frame rotated by the kinematic bank angle $\mu_K$.

Taking equation (19) into account, the estimated updated outer layer dynamics $\widehat{\boldsymbol{F}}_O$ are defined by the matrix $\widehat{\mathbf{A}}_O$ and vector $\widehat{\boldsymbol{b}}_O$ as seen in expressions (20) e (21):

$$\widehat{\mathbf{A}}_O = \begin{bmatrix} 1 & 0 \\ 0 & -1 \end{bmatrix}, \tag{20}$$

$$\widehat{\boldsymbol{b}}_O = \begin{bmatrix} \frac{(a_Z)_{\bar{K}}}{V_{TAS} \cdot \cos\beta} - (p_K)_S \cdot \tan\beta \\ \frac{(a_Y)_{\bar{K}}}{V_{TAS}} \end{bmatrix}. \tag{21}$$

Similarly, the estimated inner layer dynamics $\widehat{\boldsymbol{F}}_I$ derive from the rotational dynamics (3). Considering expressions (11)-(13), the matrix $\widehat{\mathbf{A}}_I$ and the vector $\widehat{\boldsymbol{b}}_I$ are respectively given by:

$$\widehat{\mathbf{A}}_I = \bar{q} \cdot S \cdot l \cdot \hat{\mathbf{I}}^{-1} \cdot \begin{bmatrix} \hat{C}_{L\delta_L} & 0 & \hat{C}_{L\delta_N} \\ 0 & \hat{C}_{M\delta_M} & 0 \\ \hat{C}_{N\delta_L} & 0 & \hat{C}_{N\delta_N} \end{bmatrix}, \tag{22}$$

$$\hat{\boldsymbol{b}}_I = \hat{\mathbf{I}}^{-1} \cdot \left( \bar{q} \cdot S \cdot l \cdot \begin{bmatrix} 0 & \hat{C}_{L\beta} & \hat{C}_{Lp} & 0 & \hat{C}_{Lr} \\ \hat{C}_{M\alpha} & 0 & 0 & \hat{C}_{Mq} & 0 \\ 0 & \hat{C}_{N\beta} & \hat{C}_{Np} & 0 & \hat{C}_{Nr} \end{bmatrix} \cdot \begin{bmatrix} \alpha \\ \beta \\ \frac{l}{V_{TAS}} p_K \\ \frac{l}{V_{TAS}} q_K \\ \frac{l}{V_{TAS}} r_K \end{bmatrix} - \boldsymbol{\omega}_K \times \hat{\mathbf{I}} \cdot \boldsymbol{\omega}_K \right). \quad (23)$$

## *3.2 Nonlinear Reference Model*

In order to filter and shape the command signals contained in $\boldsymbol{y}_C$, NDI-based flight controllers typically make use of linear reference models [3, 7, 8]. Since modern fighter aircraft are systems which possess complex and highly nonlinear dynamics, the use of linear reference models forces these platforms into a linear behavior, meaning that the system capabilities are not fully exploited. Another drawback of reference models designed in accordance with the classical NDI design is the fact that whenever two or more cascaded loops are employed, their dynamics are decoupled since each loop makes use of a single reference model. Additionally, linear reference models often neglect the actuator dynamics.

The abovementioned drawbacks can be circumvented by applying a nonlinear reference model which accounts for an estimation of the actuator dynamics and better recreates the real plant dynamics. It has been designed to shape the command signals in a physical way, therefore ensuring that the chosen requirements are met. The structure of the implemented nonlinear reference model is depicted in Figure 2. Unlike the classical cascaded NDI approaches, this architecture guarantees that the provided reference signals are physically related [12]. The employed reference model strategy makes use of the alternative plant representation defined in section 3.1, as well as of the time-scale separation property from the estimated outer and inner dynamic layers.

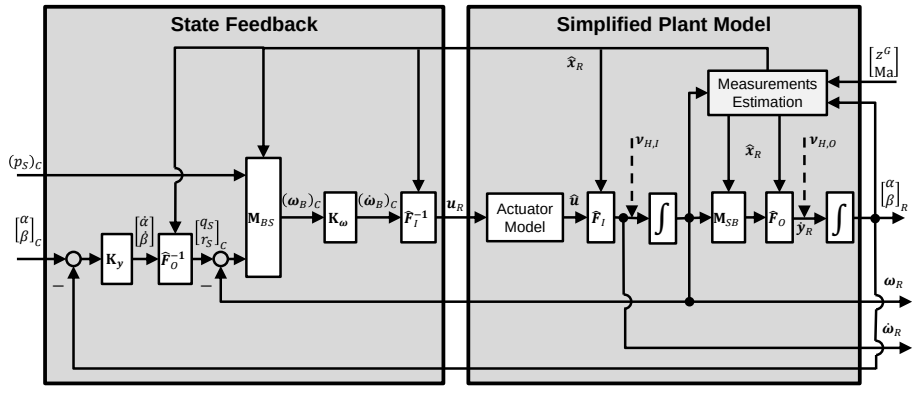


**Fig. 2** Nonlinear Reference Model Architecture

As seen in Figure 2, the nonlinear reference model contains two fundamental parts. While the left hand side subsystem consists of a state feedback controller which makes use of nonlinear dynamic inversion to guarantee that the command vector $\boldsymbol{y_C}$ is successfully tracked, the right-hand side one contains a simplified aircraft model which computes the nominal plant inner and outer layer dynamics (given by $\widehat{\boldsymbol{F}}_I$ and $\widehat{\boldsymbol{F}}_O$), taking the commanded variables and a given flight condition into account.

The diagonal matrices $\mathbf{K_y} \in \mathbb{R}^{2\times2}$ and $\mathbf{K_\omega} \in \mathbb{R}^{3\times3}$ respectively establish the feedback gains for the outer and inner dynamic layers. These gains are laid out in accordance with the performance requirements and by considering suitable time-scale separation properties. The required inner and outer layer dynamics, as well as the transformation matrices, are estimated based on the reference model states $\boldsymbol{x_R}$ and on the approximated measurements (e.g. linear accelerations). These signals are provided by the block "Measurements Estimation" and depend only on the nominal aerodynamic coefficients, aircraft altitude and Mach number. These two states exhibit slower dynamics when compared to the inner or outer layer dynamics, which means that these measurement signals can be used as external inputs to the nonlinear reference model.

In order to deal with actuator saturations, Pseudo-Control Hedging (PCH) has been employed within the implemented reference model [13]. The so-called hedging signal $\boldsymbol{\nu_H}$ is able to decelerate the reference model dynamics by taking the expected plant reaction deficit into consideration. The hedging signals which are applied to the outer and inner layer dynamics are given by:

$$\boldsymbol{\nu}_{H,O} = \widehat{\mathbf{A}}_O \cdot [(\boldsymbol{\omega}_S)_C - \widehat{\boldsymbol{\omega}}_S], \tag{24}$$

$$\boldsymbol{\nu}_{H,I} = \widehat{\mathbf{A}}_I \cdot (\boldsymbol{u}_R - \widehat{\boldsymbol{u}}). \tag{25}$$

## *3.3 NDI Baseline Controller*

Unlike traditional approaches which employ cascaded NDI-based controllers comprising two inversion loops with one reference model apiece [7, 12], this research framework considers a single nonlinear reference model (as seen in Figure 1). This modification makes it necessary to change the baseline NDI control architecture from a standard cascaded approach to a single-loop strategy [9].

As a first step, a baseline control law based on the classical cascaded NDI approach with inner and outer loops respectively corresponding to the layer dynamics provided by (16) and (17) has been derived.

$$(\boldsymbol{\omega}_S)_{BC} = \widehat{\mathbf{A}}_O^{-1} \cdot \left[\dot{\boldsymbol{y}}_R + \mathbf{K}_{P\boldsymbol{y}} \cdot \boldsymbol{e_y} + \mathbf{K}_{I\boldsymbol{y}} \cdot \boldsymbol{e}_{I\boldsymbol{y}} - \widehat{\boldsymbol{b}}_O\right] \tag{26}$$

$$\boldsymbol{u}_{BC} = \widehat{\mathbf{A}}_I^{-1} \cdot \left[ (\dot{\boldsymbol{\omega}}_B)_R + \mathbf{K}_{P\boldsymbol{\omega}} \cdot \left( \widehat{\mathbf{M}}_{BS} \cdot \begin{bmatrix} (p_S)_R \\ (\boldsymbol{\omega}_S)_{BC} \end{bmatrix} - \boldsymbol{\omega}_B \right) + \boldsymbol{K}_{Ip} \cdot e_{Ip} - \widehat{\boldsymbol{b}}_I \right] \quad (27)$$

The outer loop control law (26) includes a proportional and an integral error feedback of the outer loop states, defined by: $\boldsymbol{e_y} = ([\alpha \quad \beta]^T)_R - [\alpha \quad \beta]^T$ and $\boldsymbol{e_{Iy}} = \int \boldsymbol{e_y} \cdot dt$. The diagonal matrices $\mathbf{K}_{P\boldsymbol{y}} \in \mathbb{R}^{2\times2}$ and $\mathbf{K}_{I\boldsymbol{y}} \in \mathbb{R}^{2\times2}$ respectively contain the outer loop proportional and the integral error controller gains. Regarding the inner loop control law (27), it contains a proportional error feedback of the angular rates defined on the $B$-Frame and an integral error feedback defined by $e_{Ip} = \int [(p_B)_R - p_B] \cdot dt$. This integral element is employed in the inner loop in order to prevent the undesired presence of static error on the roll control channel (the outer loop does not include the roll control channel). The diagonal matrix $\mathbf{K}_{P\boldsymbol{\omega}} \in \mathbb{R}^{3\times3}$ and the vector $\boldsymbol{K}_{Ip} = [K_{Ip} \quad 0 \quad 0]^T$ contain the inner loop error controller gains.

The reference model pitch and yaw rates defined in the Stability Frame can be obtained by inverting the outer layer dynamics (16), as follows:

$$(\boldsymbol{\omega}_S)_R = \left(\widehat{\mathbf{A}}_O^{-1}\right)_R \cdot \left[\dot{\boldsymbol{y}}_R - \left(\widehat{\boldsymbol{b}}_O\right)_R\right]. \quad (28)$$

Assuming that the outer layer dynamics described by $\left(\widehat{\mathbf{A}}_O^{-1}\right)_R$ and $\left(\widehat{\boldsymbol{b}}_O\right)_R$ represent the estimated plant dynamics $\widehat{\boldsymbol{F}}_O$ with a certain degree of fidelity, the following approximation can be considered valid:

$$(\boldsymbol{\omega}_S)_R \approx \widehat{\mathbf{A}}_O^{-1} \cdot \left[\dot{\boldsymbol{y}}_R - \widehat{\boldsymbol{b}}_O\right]. \quad (29)$$

Making use of the latest result, equation (26) becomes the following:

$$(\boldsymbol{\omega}_S)_{BC} = (\boldsymbol{\omega}_S)_R + \widehat{\mathbf{A}}_O^{-1} \cdot \left[\mathbf{K}_{P\boldsymbol{y}} \cdot \boldsymbol{e_y} + \mathbf{K}_{I\boldsymbol{y}} \cdot \boldsymbol{e_{Iy}}\right]. \quad (30)$$

Updating equation (27) with expression (30) yields the final baseline control law:

$$\boldsymbol{u}_{BC} = \widehat{\mathbf{A}}_I^{-1} \cdot \left[ \underbrace{(\dot{\boldsymbol{\omega}}_B)_R + \mathbf{K}_{P\boldsymbol{\omega}} \cdot \boldsymbol{e_\omega} + \begin{bmatrix} K_{Ip} \cdot e_{Ip} \\ \mathbf{K}_{P\boldsymbol{y}}^* \cdot \boldsymbol{e_y} + \mathbf{K}_{I\boldsymbol{y}}^* \cdot \boldsymbol{e_{Iy}} \end{bmatrix}}_{\boldsymbol{\nu}_{BC}} - \widehat{\boldsymbol{b}}_I \right], \quad (31)$$

where $\mathbf{K}_{P\boldsymbol{y}}^* = \mathbf{K}_{P\boldsymbol{\omega}} \cdot \widehat{\mathbf{M}}_{BS}^* \cdot \widehat{\mathbf{A}}_O^{-1} \cdot \mathbf{K}_{P\boldsymbol{y}}$, $\mathbf{K}_{I\boldsymbol{y}}^* = \mathbf{K}_{P\boldsymbol{\omega}} \cdot \widehat{\mathbf{M}}_{BS}^* \cdot \widehat{\mathbf{A}}_O^{-1} \cdot \mathbf{K}_{I\boldsymbol{y}}$ and the angular rate feedback error is given by $\boldsymbol{e_\omega} = (\boldsymbol{\omega}_B)_R - \boldsymbol{\omega}_B$. The transformation matrix $\widehat{\mathbf{M}}_{BS}^* \in \mathbb{R}^{3\times2}$ converts the angular rates $[q_S \quad r_S]^T$ into $\boldsymbol{\omega}_B$, assuming that the roll rate contribution in the stability frame is zero. It can be seen from expression (31) that by employing this control strategy, the chosen baseline control law is not af-

fected by the outer layer nonlinearities $\widehat{\boldsymbol{b}}_O$, which might lead to benefits in terms of robustness. Knowing that $\dot{\boldsymbol{\omega}}_B = \widehat{\mathbf{A}}_I \cdot \boldsymbol{u}_{BC} + \widehat{\boldsymbol{b}}_I$ (17) and taking expression (31) into account, the error dynamics of the closed-loop system can be given by:

$$\begin{bmatrix} \dot{\boldsymbol{e}}_{\boldsymbol{\omega}} \\ \dot{e}_{Ip} \\ \dot{\boldsymbol{e}}_{\boldsymbol{Iy}} \\ \dot{\boldsymbol{e}}_{\boldsymbol{y}} \end{bmatrix} = \underbrace{\begin{bmatrix} -\mathbf{K}_{P\boldsymbol{\omega}} & -\boldsymbol{K}_{Ip} & -\mathbf{K}^*_{\boldsymbol{Iy}} & -\mathbf{K}^*_{\boldsymbol{Py}} \\ \boldsymbol{I}^* & 0 & \mathbf{0}_{1\times 2} & \mathbf{0}_{1\times 2} \\ \mathbf{0}_{2\times 3} & \mathbf{0}_{2\times 1} & \mathbf{0}_{2\times 2} & \mathbf{I}_{2\times 2} \\ \widehat{\mathbf{A}}_O \cdot \widehat{\mathbf{M}}^*_{SB} & \mathbf{0}_{2\times 1} & \mathbf{0}_{2\times 2} & \mathbf{0}_{2\times 2} \end{bmatrix}}_{\mathbf{A}_{err}} \cdot \begin{bmatrix} \boldsymbol{e}_{\boldsymbol{\omega}} \\ e_{Ip} \\ \boldsymbol{e}_{\boldsymbol{Iy}} \\ \boldsymbol{e}_{\boldsymbol{y}} \end{bmatrix} + \boldsymbol{\Delta}_{appr}, \tag{32}$$

where $\boldsymbol{I}^* = [1 \quad 0 \quad 0]$, $\widehat{\mathbf{M}}^*_{SB} \in \mathbb{R}^{2\times 3}$ is a transformation matrix which converts $\boldsymbol{\omega}_B$ into $[q_S \quad r_S]^T$, and $\boldsymbol{\Delta}_{appr} \in \mathbb{R}^4$ is the approximation error deriving from the difference between real and approximated reference model plant dynamics.

## *3.4 Adaptive Augmentation of the NDI Baseline Controller*

In order to deal with potential uncertainties deriving from differences between the estimated and the real plant dynamics, the implemented baseline controller is augmented with an adaptive element based on MRAC architecture [10]. A projection algorithm is also implemented in order to prevent the adaptive parameters from drifting [14]. The overall control structure, including the baseline controller and the adaptive element is shown in Figure 3.

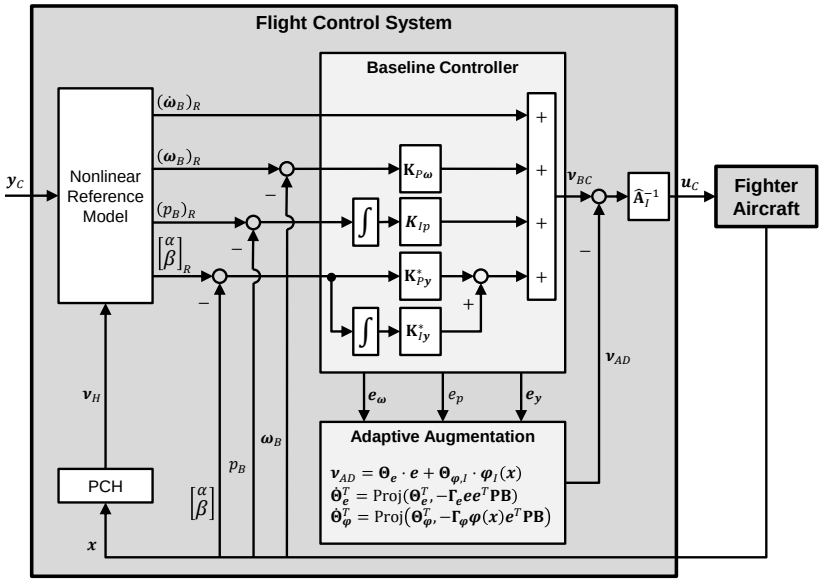


**Fig. 3** NDI Baseline Control Architecture with Adaptive Augmentation

After the inclusion of an adaptive contribution $\boldsymbol{\nu}_{AD}$ and once again remembering that $\dot{\boldsymbol{\omega}}_B = \widehat{\mathbf{A}}_I \cdot \boldsymbol{u}_{BC} + \widehat{\boldsymbol{b}}_I$ (17), the former closed-loop dynamics given by (31) are updated as follows:

$$\dot{\boldsymbol{\omega}} = \dot{\boldsymbol{\omega}}_R + \mathbf{K}_{P\boldsymbol{\omega}} \cdot \boldsymbol{e}_{\boldsymbol{\omega}} + \begin{bmatrix} K_{Ip} \cdot e_{Ip} \\ \mathbf{K}^*_{P\boldsymbol{y}} \cdot \boldsymbol{e}_{\boldsymbol{y}} + \mathbf{K}^*_{I\boldsymbol{y}} \cdot \boldsymbol{e}_{I\boldsymbol{y}} \end{bmatrix} + \boldsymbol{b}_I - \widehat{\boldsymbol{b}}_I + \boldsymbol{\Delta}_{\boldsymbol{\omega}} - \boldsymbol{\nu}_{AD}, \quad (33)$$

where $\boldsymbol{\Delta}_{\boldsymbol{\omega}} \in \mathbb{R}^{3\times1}$ includes the deviation between nominal model and real plant due to uncertainties. Taking expressions (32) and (33) into account, the closed-loop error dynamics are given by:

$$\begin{bmatrix} \dot{\boldsymbol{e}}_{\boldsymbol{\omega}} \\ \dot{e}_{Ip} \\ \dot{\boldsymbol{e}}_{I\boldsymbol{y}} \\ \dot{\boldsymbol{e}}_{\boldsymbol{y}} \end{bmatrix} = \mathbf{A}_{err} \cdot \underbrace{\begin{bmatrix} \boldsymbol{e}_{\boldsymbol{\omega}} \\ e_{Ip} \\ \boldsymbol{e}_{I\boldsymbol{y}} \\ \boldsymbol{e}_{\boldsymbol{y}} \end{bmatrix}}_{\boldsymbol{e}} + \underbrace{\begin{bmatrix} \boldsymbol{I}_{3\times3} \\ \mathbf{0}_{1\times3} \\ \mathbf{0}_{2\times3} \\ \mathbf{0}_{2\times3} \end{bmatrix}}_{\mathbf{B}_{err}} \cdot \boldsymbol{\nu}_{ad} - \begin{bmatrix} \boldsymbol{b}_I - \widehat{\boldsymbol{b}}_I + \boldsymbol{\Delta}_{\boldsymbol{\omega}} \\ 0 \\ \mathbf{0}_{2\times1} \\ \boldsymbol{\Delta}_O \end{bmatrix} + \boldsymbol{\Delta}_{appr}, \quad (34)$$

with $\boldsymbol{\Delta}_O \in \mathbb{R}^{2\times1}$ being defined as the vector containing the outer layer unmatched uncertainties which derive from the error dynamics.

Within the current control problem, only the matched inner loop uncertainties $\boldsymbol{\Delta}_{\boldsymbol{\omega}}$ can be dealt with by making use of adaptation. A new description of the model uncertainty including the error $\boldsymbol{b}_I - \widehat{\boldsymbol{b}}_I$ can be given by the following parameterization:

$$\boldsymbol{\Theta}^*_{\boldsymbol{\varphi}} \cdot \boldsymbol{\varphi}(\boldsymbol{x}) = \boldsymbol{b}_I - \widehat{\boldsymbol{b}}_I + \boldsymbol{\Delta}_{\boldsymbol{\omega}}, \quad (35)$$

where $\boldsymbol{\Theta}^*_{\boldsymbol{\varphi}}$ and $\boldsymbol{\varphi}(\boldsymbol{x})$ respectively represent the ideal constant parameter matrix and the nonlinear regressor vector. For example, the parameterization of the pitch control channel is given by the following expression:

$$(b_I)_q - \left(\widehat{b}_I\right)_q + \Delta_q = \underbrace{\begin{bmatrix} \frac{1}{I_{yy}} \cdot S \cdot l & \frac{1}{I_{yy}} \cdot S \cdot l^2 \cdot C_{Mq} & \frac{I_{xz}}{I_{yy}} & \frac{(I_{zz}-I_{xx})}{I_{yy}} \end{bmatrix}}_{(\boldsymbol{\theta}^*_{\boldsymbol{\varphi}})_q} \cdot \underbrace{\begin{bmatrix} \bar{q} \cdot C_{M\alpha} \cdot \alpha \\ \bar{q} \cdot \frac{q_K}{v_{TAS}} \\ r_K^2 - p_K^2 \\ p_K \cdot r_K \end{bmatrix}}_{\boldsymbol{\varphi}_q(\boldsymbol{x})}. \quad (36)$$

Taking reference [10] into account, a gradient based parameter update law for the parameter matrix has been chosen.

$$\dot{\boldsymbol{\Theta}}^T_{\boldsymbol{\varphi}} = \mathrm{Proj}\left(\boldsymbol{\Theta}^T_{\boldsymbol{\varphi}}, -\boldsymbol{\Gamma}_{\boldsymbol{\varphi}} \boldsymbol{\varphi}(\boldsymbol{x}) \boldsymbol{e}^T \mathbf{P}\mathbf{B}\right) \quad (37)$$

In the expression above, $\boldsymbol{\Gamma}_{\boldsymbol{\varphi}}$ provide the constant learning rates, which describe the growth rate of the parameter estimate $\boldsymbol{\Theta}_{\boldsymbol{\varphi}}$. The learning rates have been laid

out by considering the physical limitations of the plant. The matrix $\mathbf{P}$ is simply given by the solution of the following Lyapunov equation:

$$\mathbf{A}_{err}^{T}(\boldsymbol{x_0}) \cdot \mathbf{P} + \mathbf{P} \cdot \mathbf{A}_{err}(\boldsymbol{x_0}) = -\mathbf{I}. \tag{38}$$

As the dynamics matrix $\mathbf{A}_{err}(\boldsymbol{x})$ varies with Mach number, aircraft altitude and with the aerodynamic angles, it has slower dynamics than the inner and outer layers (it is assumed that the aerodynamic angles have a minor impact in the dynamics matrix). Due to this fact, the matrix $\mathbf{A}_{err}(\boldsymbol{x_0})$ can be used to approximate $\mathbf{A}_{err}(\boldsymbol{x})$, and is thus be employed in expression (38) to compute $\mathbf{P}$. Since the unmatched uncertainties may lead to an undesired adaptive parameter growth, a projection algorithm "Proj(.)" is used by the parameter update laws to ensure that the adaptive parameters remain within predefined bounds [14].

## 4 Simulation Results

This section contains the simulation results which can be used to assess the benefits of the employed control strategy. In order to demonstrate the potential of the implemented flight control system, an aggressive maneuver consisting of step commands in the roll and pitch channels has been chosen. The fighter aircraft must be able to track an angle of attack $\alpha_C$ step command (corresponding to the maximum allowable load factor $n_Z = 9$ g), followed two seconds later by a roll rate $(p_S)_C$ step command with amplitude 75 degrees per second. The sideslip angle command is a constant signal $\beta_C = 0°$. The objective is to obtain a roll channel response as close as possible to the one provided by a first-order linear system defined by a time constant $T_S$ and a pitch response as similar as possible to the one provided by a second-order linear system defined by a natural frequency $\omega_0$ and by a damping coefficient of 0.7. The desired values of $T_S$ and $\omega_0$ vary with the Calibrated Airspeed. Additionally, the static error must be kept at a minimum.

Figure 4 contains the baseline controller response after carrying out the aforementioned maneuver under nominal conditions at four different flight envelope points. Like all figures comprised in this chapter, it also depicts the different control surface deflections and its respective rates. It can be assessed that, for each considered flight envelope point, the implemented baseline controller is able to successfully track the demanded signals with relatively short rise and settling times, as well as minimum static error. Additionally, it has been verified that the control surfaces only hit their physical limits during the transient behavior. However, the response in the pitch channel corresponding to the most demanding flight condition (low altitude, low speed – blue line) is not well damped.

In order to investigate the FCS performance in the case where deviations between the real and the estimated model exist, four uncertainty combinations have been chosen. These can be seen on Table 1.

**Table 1.** Uncertainty Combinations Applied During the Simulation Runs.

| Variable | UC 1 | UC 2 | UC 3 | UC 4 |
|---|---|---|---|---|
| $m$ | -2000 kg | +2000 kg | +2000 kg | -2000 kg |
| $x^G$ | -2% | +2% | +2% | -2% |
| $C_{M\alpha}$ | -0.05 rad$^{-1}$ | +0.05 rad$^{-1}$ | +0.05 rad$^{-1}$ | +0.05 rad$^{-1}$ |
| $C_{L\beta}, C_{N\beta}$ | -0.05 rad$^{-1}$ | -0.05 rad$^{-1}$ | +0.05 rad$^{-1}$ | +0.05 rad$^{-1}$ |
| $C_{M\delta_M}$ | -30% | -30% | -30% | -30% |
| $C_{L\delta_L}, C_{L\delta_N}, C_{N\delta_L}, C_{N\delta_N}$ | -30% | -30% | +30% | +30% |
| $I_{xx}$ | -20% | -20% | +20% | +20% |
| $I_{yy}$ | -20% | -20% | +20% | -20% |
| $I_{zz}$ | +20% | -20% | +20% | -20% |

For each of the abovementioned uncertainty combinations, a simulation run using the combined maneuver comprising lateral and longitudinal commands has been performed at flight condition $z_E^G = 10$ km and $\mathrm{Ma} = 0.7$. Moreover, strong turbulence effects (simultaneous wind gusts from all directions) have been taken into account during the simulation runs. With the purpose of assessing the benefits of the adaptive augmentation, the uncertainty combinations and the turbulence effects have also been applied to the baseline controller.

Figure 5 depicts the simulation results for the case when only the baseline controller is active (adaptation switched off), whereas Figure 6 shows the performance of the augmented baseline controller. Even though the baseline architecture (Figure 5) leads to a stable closed-loop behavior for every considered uncertainty combination, its tracking capabilities are insufficient when compared to the desired system response (e.g. in terms of static error and overshoot in $\alpha_A$).

As seen in Figure 6, a superior tracking performance and a better match to the desired system response is obtained when the adaptive augmented controller is employed. In this case, the static error and overshoot have been reduced at each uncertainty combination. Additionally, it can be seen that the control surfaces seldom reach their physical limits.

16

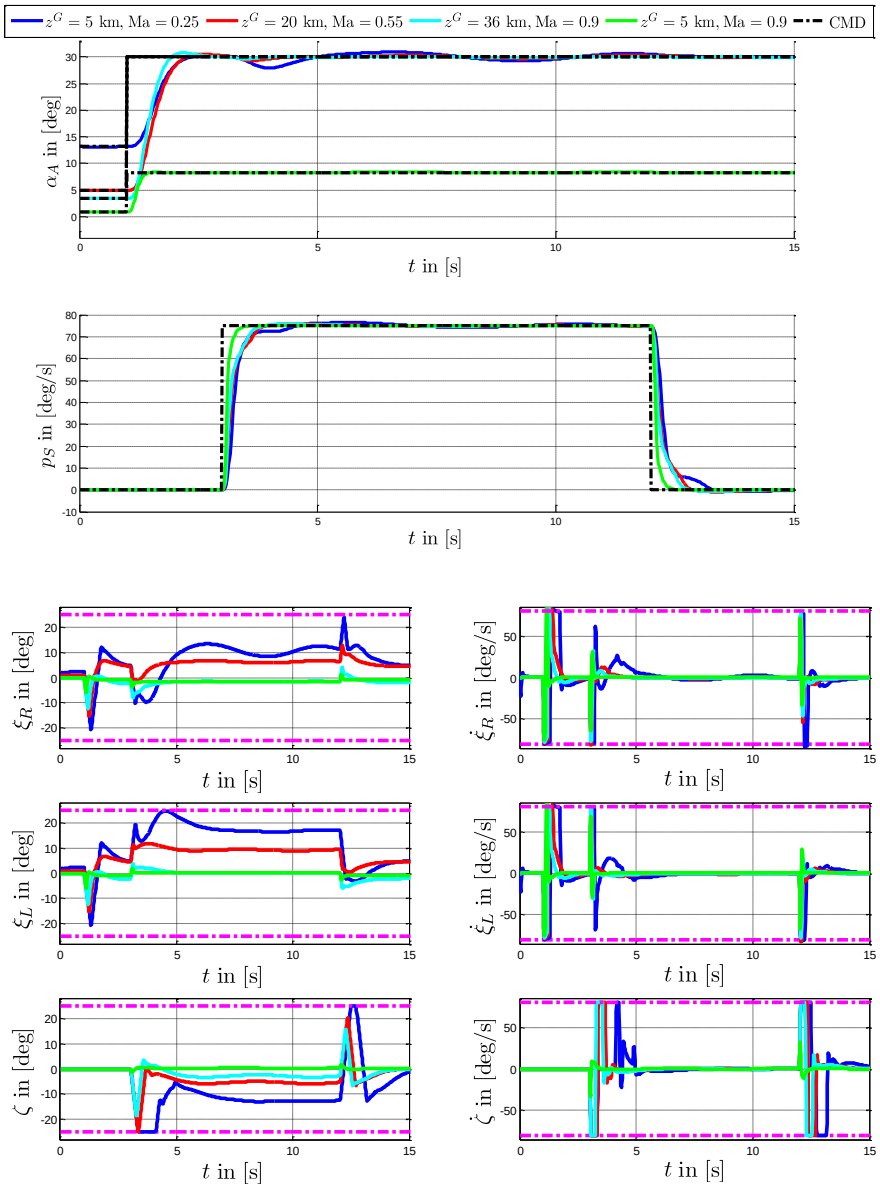


**Fig. 4** Baseline Controller Performance for a Combined Longitudinal and Lateral Maneuver at Four Different Flight Envelope Points and Corresponding Actuator Behavior

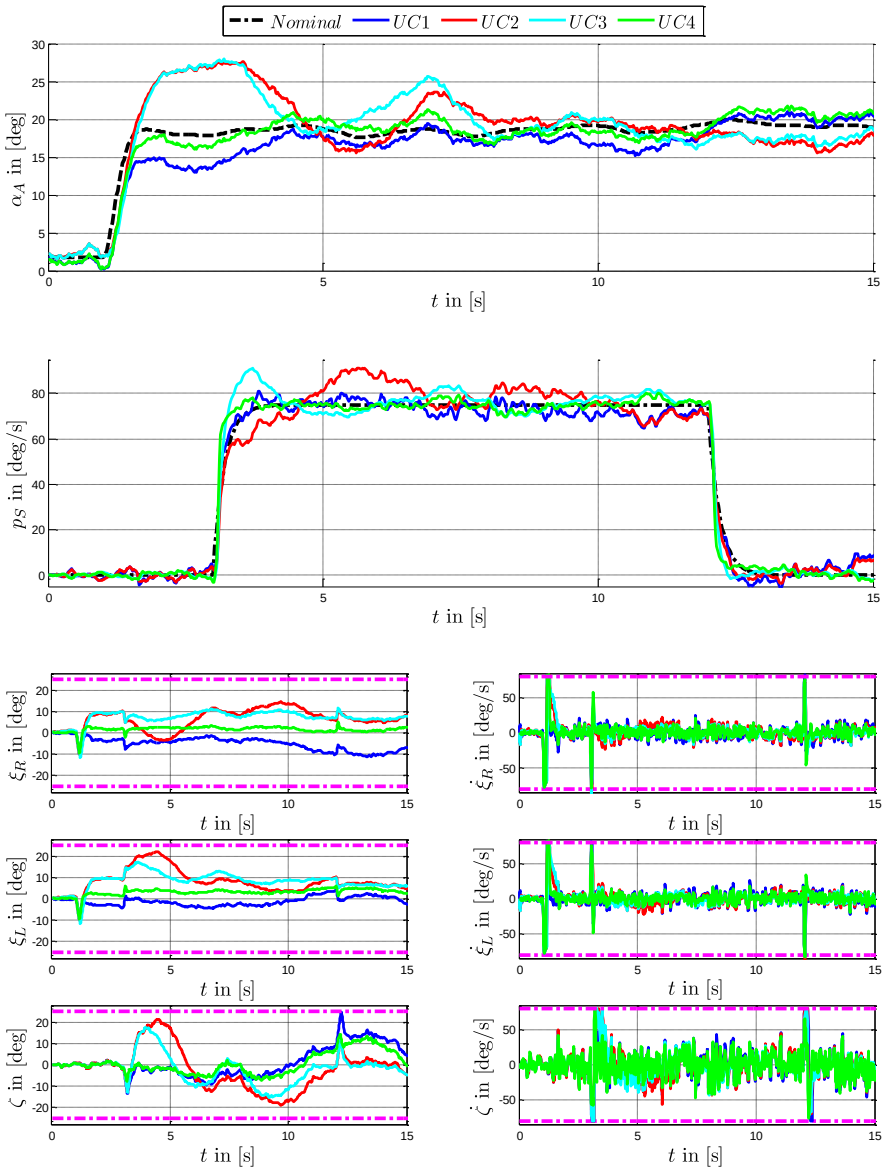


**Fig. 5** Combined Longitudinal and Lateral Maneuver Obtained with the Baseline Controller at $h = 10$ km & $Ma = 0.7$ for the Selected Four Uncertainty Combinations and in Presence of Strong Turbulence

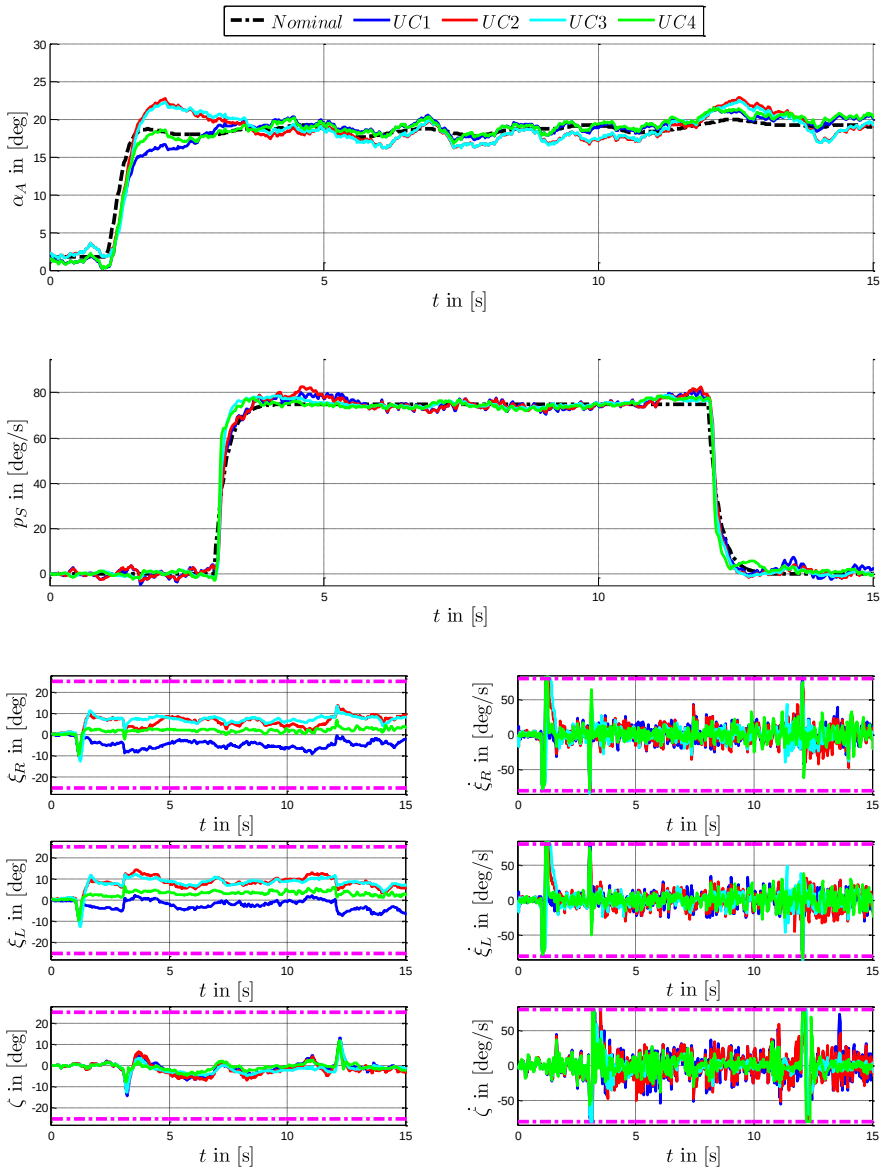


**Fig. 6** Combined Longitudinal and Lateral Maneuver Obtained with the Adaptive Augmented Baseline Controller at $h = 10$ km & $Ma = 0.7$ for the Selected Four Uncertainty Combinations and in Presence of Strong Turbulence

## 5 Conclusion

In this document, the adaptive augmentation of a modern fighter aircraft autopilot has been considered. The NDI baseline controller makes use of a nonlinear reference model which includes the main plant nonlinearities and an estimation of the actuator dynamics, thus better representing the real plant dynamics. Such a reference model allows the control designer to shape the command signals in a physical way, therefore ensuring that the chosen requirements are met.

Since the baseline controller presents an almost linear behavior, the requirements for using MRAC augmentation are fulfilled. In order to prevent parameter drift caused by unmodeled dynamics, a projection algorithm has been used.

The designed flight control system is able to successfully perform a demanding maneuver, tracking the commanded signals in the presence of large uncertainties and strong turbulence.

**Acknowledgments** The authors gratefully acknowledge that the presented work was supported by project NICE (Ref. A-0933-RT-GC) which has been coordinated by the European Defence Agency (EDA) and funded by eleven contributing Members (Cyprus, France, Germany, Greece, Hungary, Italy, Norway, Poland, Slovakia, Slovenia and Spain) under the framework of the Joint Investment Programme on Innovative Concepts and Emerging Technologies (JIP-ICET).

## References

1. Wang, Q., Stengel, R. F.: Robust Nonlinear Flight Control of a High-Performance Aircraft. In: IEEE Transactions on Control Systems Technology, Vol. 13, No. 1 (2005)
2. Schumacher, C., Johnson, J. D.: PI Control of a Tailless Fighter Aircraft with Dynamic Inversion and Neural Networks. In: Proceedings of the American Control Conference (1999)
3. Johnson, E. N., Calise, A. J., Corban, J. E.: Adaptive Guidance and Control for Autonomous Launch Vehicles. In: Proceedings of the IEEE Aerospace Conference, Vol. 6 (2001)
4. Miller, C. J.: Nonlinear Dynamic Inversion Baseline Control Law: Flight-Test Results for the Full-scale Advanced Systems Testbed F/A-18 Airplane. In: AIAA Guidance, Navigation, and Control Conference (2011)
5. Holzapfel, F.: Nichtlineare adaptive Regelung eines unbemannten Fluggerätes. Ph.D. Thesis, Technische Universität München, Munich (2004)
6. Bugaski, D. J., Enns, D. F., Elgersma, M. R.: A Dynamic Inversion Based Control with Application to the F-18 HARV. In: Proceedings of the AIAA Guidance, Navigation and Control Conference (1990)
7. Ito, D., Georgie, J., Valasek, J., Ward, D. T.: Reentry Vehicle Flight Controls Design Guidelines: Dynamic Inversion. In: 2010 IEEE International Symposium on Intelligent Control (2010)
8. Calise, A. J., Lee, S., Sharma, M.: Direct Adaptive Reconfigurable Control of a Tailless Fighter Aircraft. In: AIAA-98-4108 (1998)
9. Peter, F., Leitão, M., Holzapfel, F.: Adaptive Augmentation of a New Baseline Control Architecture for Tail-Controlled Missiles Using a Nonlinear Reference Model. In: AIAA Guidance, Navigation and Control Conference (2012)

10. Narendra, K. S., Annaswamy, A. M.: Stable Adaptive Systems. Dover Publications, Mineola (2005)
11. U.S. Standard Atmosphere 1976, U.S. Government Printing Office, Washington, D.C. (1976)
12. Reiner, J., Balas, G. M., Garrard, W. L.: Flight Control Design Using Robust Dynamic Inversion and Time-scale Separation. In: Automatica, Vol. 32, No. 11 (1996)
13. Johnson, E. N., Calise, A.J.: Pseudo-Control Hedging: A New Method for Adaptive Control. In: Advances in Navigation Guidance and Control Technology Workshop (2000)
14. Gibson, T. E., Matsutani, M., Crespo, L. G., Annaswamy, A. M.: Internal Algorithm Monitor for Adaptive Systems. In: AIAA Infotech Aerospace Conference (2010)